

RhythmFormer: Extracting rPPG Signals Based on Hierarchical Temporal Periodic Transformer

Bochao Zou, Zizheng Guo, Jiansheng Chen, Huimin Ma*

University of Science and Technology Beijing

zoubochao@ustb.edu.cn, guozizheng@xs.ustb.edu.cn, {jschen, mhmpub}@ustb.edu.cn

Abstract

Remote photoplethysmography (rPPG) is a non-contact method for detecting physiological signals based on facial videos, holding high potential in various applications such as healthcare, affective computing, anti-spoofing, etc. Due to the periodicity nature of rPPG, the long-range dependency capturing capacity of the Transformer was assumed to be advantageous for such signals. However, existing approaches have not conclusively demonstrated the superior performance of Transformer over traditional convolutional neural network methods, this gap may stem from a lack of thorough exploration of rPPG periodicity. In this paper, we propose RhythmFormer, a fully end-to-end transformer-based method for extracting rPPG signals by explicitly leveraging the quasi-periodic nature of rPPG. The core module, Hierarchical Temporal Periodic Transformer, hierarchically extracts periodic features from multiple temporal scales. It utilizes dynamic sparse attention based on periodicity in the temporal domain, allowing for fine-grained modeling of rPPG features. Furthermore, a fusion stem is proposed to guide self-attention to rPPG features effectively, and it can be easily transferred to existing methods to enhance their performance significantly. RhythmFormer achieves state-of-the-art performance with fewer parameters and reduced computational complexity in comprehensive experiments compared to previous approaches. The codes are available at <https://github.com/zizheng-guo/RhythmFormer>.

1. Introduction

Blood Volume Pulse (BVP) is an important physiological signal, further allowing for the extraction of key vital signs such as heart rate (HR) and heart rate variability (HRV). Photoplethysmography (PPG) is a non-invasive monitoring method that utilizes optical means to measure changes in blood volume within living tissues. The physio-

*Corresponding author

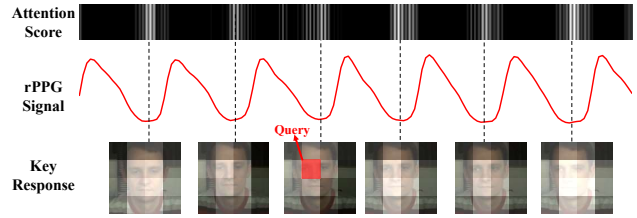


Figure 1. Sparsity in attention due to periodicity. Given the red block as a Query, the global spatio-temporal correlations are computed. Brighter regions in the attention score and key responses in the frame indicate stronger attention. From the figure, it is evident that the brightness of the key responses in the frame is predominantly concentrated in the skin area, while the brightness in the attention score is mainly focused on the troughs (regions with the same phase as the Query). The attention scores exhibit a notable sparsity.

logical mechanism underlying BVP extraction from PPG is rooted in variations in light absorption and scattering due to changes in blood volume during cardiac contraction and relaxation in subcutaneous blood vessels. These variations result in periodic color signal alterations on imaging sensors, imperceptible to the human eye [3, 45]. Traditionally, BVP extraction required the use of contact sensors, introducing inconveniences and limitations. In recent years, non-contact methods for extracting BVP information, specifically remote photoplethysmography (rPPG), have garnered increasing attention [12, 28, 29].

Early research on rPPG primarily relied on signal processing based methods to analyze skin, typically facial, videos for extracting periodic signals [9, 10, 19, 21, 33, 34, 45, 47, 48]. However, due to the weak amplitude of rPPG signals and the presence of strong noise from environmental factors like lighting and motion, achieving high accuracy solely through signal processing in complex environments is challenging. With the advancement of deep learning, there is a growing trend towards data-driven methods. In recent years, significant attention has been directed towards the transformer within the rPPG domain. Compared

to CNNs, transformers excel in capturing long-range dependency. This is particularly advantageous for extracting BVP signals characterized by quasi-periodicity and simultaneous existence across all skin regions. However, existing research has not convincingly demonstrated that transformers outperform traditional CNNs. This may be attributed to the quadratic scaling exhibited by Transformers with sequence length [1], a challenge further compounded by the high dimensionality of video. Past work typically transformed inputs into coarse-grained tokens, and due to artifacts and head movement [56, 57], these coarse tokens inevitably encompass both regions rich in rPPG information and regions with significant noise. The introduction of noise through coarse-grained extraction, combined with the inherently weak nature of rPPG signals, results in a low signal-to-noise ratio.

To address the aforementioned issues, we observe that: as shown in Figure 1, spatially, numerous regions (including the background and areas without exposed skin) are irrelevant to rPPG information. Temporally, the attention of rPPG displays notable temporal sparsity. We anticipate attention to concentrate on skin regions with similar temporal phases, making a substantial portion of self-attention computations invaluable. Based on the observed characteristics, we propose RhythmFormer, which explicitly leverages the periodicity of rPPG. RhythmFormer explores periodic features at multiple temporal scales, utilizing the temporal sparsity induced by periodicity. Initially, computing spatio-temporal correlations within a large spatio-temporal receptive field aims to aggregate regions with high phase similarity temporally and rich rPPG signals spatially. Subsequently, finer-grained feature extraction is conducted from these high-correlation regions. Concurrently, in addressing the challenge of pronounced self-attention deviation due to the inherently weak nature of rPPG features, we devised the fusion stem. This design allows frame-level representations to be aware of BVP wave variations, effectively guiding the self-attention mechanism.

The main contributions are as follows:

1. We propose RhythmFormer, a fully end-to-end method that explicitly leverages periodicity to design the periodic sparse attention mechanism, which finely extracts periodic rPPG features across multiple temporal scales.

2. We propose a plug-and-play fusion stem module, enabling frame-level representation awareness of BVP wave variations. This module can be seamlessly integrated into other methods, thereby significantly improving the performance of existing approaches.

3. We conduct extensive experiments on both intra-dataset and cross-dataset scenarios. Results demonstrate that our method outperforms previous state-of-the-art methods in comprehensive testing with fewer parameters and reduced computational requirements.

2. Related Work

2.1. Remote Physiological Estimation

Previous research on rPPG predominantly relied on traditional signal processing methods to analyze facial videos for extracting their periodic signals [9, 10, 19, 21, 33, 34, 45, 47, 48]. With the advancement of deep learning, an increasing number of data-driven approaches have emerged, showcasing a trend in backbones transitioning from 2D CNNs [3, 6, 22, 30–32, 39] to 3D CNNs [18, 20, 42, 51, 52, 60] and further to transformer [13, 15, 23, 36, 37, 54, 56, 57, 59]. The superiority of 3D CNNs over 2D CNNs arises from their enhanced capability to capture temporal information for tasks like rPPG. In comparison to 3D CNNs, transformers excel in capturing long-range spatial and temporal correlations, making them particularly advantageous for extracting quasi-periodic PPG signals. However, existing transformer-based methods are either non-end-to-end, requiring a complex preprocessing procedure and potentially overlooking global contextual cues outside predefined ROIs [13, 15, 37, 59], or they are based on Video Transformer, tending to extract features at a coarse granularity [36, 56, 57], or they are based on Vision Transformer, which may disregard long-range temporal relationships [23]. None of these approaches has demonstrated a significant performance advantage over CNN methods.

2.2. Sparse Attention Mechanisms

The conventional attention mechanism poses a significant computational burden and demands substantial memory resources as it involves pair-wise token interaction across all spatial-temporal locations [1, 44]. Numerous solutions have been proposed to address this issue [5, 8, 46]. Sparse attention has gained recent popularity, particularly fueled by the remarkable success of the Swin Transformer [25]. Subsequent works have introduced various hand-crafted sparse attention, such as expanding windows [43, 49] or cross-shaped windows [11]. Some endeavors aim to adapt sparse patterns to data, exemplified by DAT [50], TCFormer [58], and DPT [4]. Biformer [61] explores a dynamic, query-aware sparse attention mechanism, introducing new possibilities for sparse attention. Previous rPPG-related works [13, 23, 56, 57] primarily employed coarse-grained global attention without incorporating sparse attention mechanisms. This might be attributed to two potential reasons: One is that rPPG information is present in the skin regions across all temporal periods, making it difficult to achieve sparse attention through hand-crafted static attention mechanisms; Another is that most of the sparse attention mechanisms mentioned above are designed for use on two-dimensional images, posing a challenge in their application to three-dimensional video data.

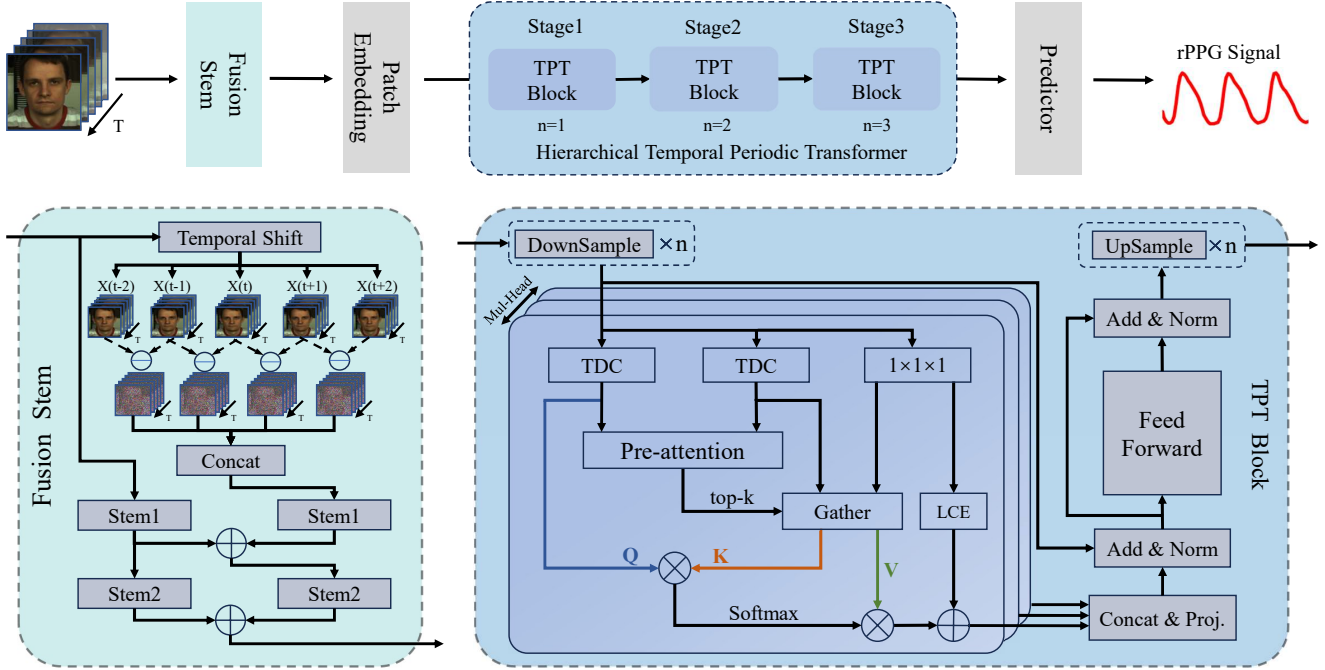


Figure 2. Framework of RhythmFormer. It consists of fusion stem, patch embedding, Hierarchical Temporal Periodic Transformer, and rPPG predictor head. The proposed Hierarchical Temporal Periodic Transformer consists of three stages and each stage contains a TPT Block with a sampling coefficient of n , where n is the number of the sample block.

3. Methodology

In Section 3.1, the general framework of RhythmFormer will be presented, followed by the Fusion Stem in Section 3.2 and the Hierarchical Temporal Periodic Transformer (TPT) in Section 3.3. Lastly, Section 3.4 introduces the proposed HR hybrid loss.

3.1. The general framework of RhythmFormer

As shown in Figure 2, RhythmFormer primarily consists of a fusion stem, the patch embedding, a Hierarchical Temporal Periodic Transformer, and an rPPG prediction head (MLP). We utilize the fusion stem to integrate the difference frame with the raw frame, enabling the capability to be aware of frame-level rPPG information. This enhances the representation features and guides the transformer to focus on the rPPG signal. Specifically, given an RGB video input $X \in \mathbb{R}^{3 \times T \times H \times W}$, $X_{stem} = fusion_stem(X)$, where $X_{stem} \in \mathbb{R}^{C \times T \times H/4 \times W/4}$, and C, T, W, H indicate channel, sequence length, width, and height, respectively.

Next, the output of the fusion stem will be divided into non-overlapping tokens through patch embedding. This spatially aggregates neighboring semantic information while reducing the computational cost of the transformer. Specifically, given the input X_{stem} , the output of patch embedding is denoted as X_{token} , where $X_{token} \in \mathbb{R}^{C \times T \times H/16 \times W/16}$. The token number is $T \times H/16 \times$

$W/16$. There is no explicit position embedding. Instead, the relative positional cues are implicitly provided through the fusion stem, the hidden layer convolution in the feed-forward, and the local context enhancement (LCE) term in the periodic sparse attention [35].

Subsequently, the output of patch embedding will be fed into the Hierarchical Temporal Periodic Transformer, extracting rPPG features at a fine granularity from different time scales through periodic sparse attention mechanisms. Specifically, this involves three TPT Blocks, where the input and output of the i_{th} block are denoted as $X_{block_i} \in \mathbb{R}^{C \times T \times H/16 \times W/16}$. Finally, the rPPG features will be projected into BVP waves through a prediction head.

3.2. Fusion Stem

Handling the conflict between strong noise and weak features is a key issue in the rPPG task. Some non-end-to-end methods [12, 13, 27, 32, 37] use color space transformations based on ROI regions to obtain spatio-temporal signal maps. However, these methods ignore global contextual cues outside the predefined ROIs and require strict pre-processing steps, making them less suitable for deployment on mobile devices. In previous end-to-end rPPG research, there are primarily two ways to take video input. The first one is to directly use raw frames as input [51, 56, 57]. The second one is to input the normalized frame difference, while also inputting the raw frames to provide atten-

tion. The difference frame is guided by the original raw frame to focus on the skin region [3, 22, 60]. The difference frame holds an advantage as it effectively removes the influence of fixed component noise (e.g., skin color and camera noise). However, other noise sources such as ambient light and motion artifacts still exist. This low signal-to-noise ratio poses a significant challenge for transformer models based on self-attention mechanisms. When using raw frames as input, self-attention struggles to focus on the subtle changes in skin color compared to more prominent facial features. There is a higher correlation between similar spatial regions in each frame, rather than between temporally phase-similar regions. Consequently, a significant proportion of the self-attention scores originate from facially similar regions rather than capturing the rPPG features manifested by skin color changes, leading to a substantial deviation between the actual focus and the desired ones.

Based on this, we propose the fusion stem that integrates the difference frame into the raw frame, enabling frame-level representation to be aware of BVP wave variations. This fusion stem effectively enhances rPPG features with minimal additional computational cost. The inclusion of this module not only guides the self-attention mechanism of the transformer to reinforce its focus on rPPG representation but also achieves outstanding performance across all end-to-end methods [see Section 4.5].

As shown in Figure 2, for an input video $X \in \mathbb{R}^{3 \times T \times H \times W}$, first temporal shift is applied to obtain X_{t-2} , X_{t-1} , X_t , X_{t+1} and X_{t+2} . Then, the differences between consecutive frames are computed in chronological order, resulting in D_{-2} , D_{-1} , D_1 and D_2 . These difference frames, along with the raw frames, are passed through Stem_1 for primary feature extraction. Stem_1 consists of a 2D convolution with a kernel size of (5×5) , cascaded by batch normalization(BN), ReLU, and MaxPool.

$$X_{diff} = Stem_1(Concat(D_{-2}, D_{-1}, D_1, D_2)) \quad (1)$$

$$X_{origin} = Stem_1(X_t) \quad (2)$$

Then the features of the difference video and the raw video are merged and the feature representation is further enhanced through Stem_2, which also consists of a 2D convolution with a kernel size of (3×3) , cascaded by BN and ReLU.

$$X_{stem} = \alpha * Stem_2(X_{origin}) + \beta * Stem_2(\alpha * X_{origin} + \beta * X_{diff}) \quad (3)$$

The fusion coefficients α and β are both set to 0.5 experimentally.

3.3. Hierarchical Temporal Periodic Transformer

Past studies [7, 14, 16] have demonstrated the effectiveness of modeling periodic tasks with multiple temporal

scales, primarily extracting temporal information through concatenation from paths at various scales. In the context of rPPG tasks, similar to many spatial multi-scale models [25, 43], we believe that a pyramid-shaped hierarchical multi-scale learning can facilitate the provision of information from earlier learned scales to later learned scales. The proposed Hierarchical Temporal Periodic Transformer consists of three stages. It first reinforces inter-frame rPPG features at a smaller time scale and then models periodic features at a larger time scale, effectively reducing noise interference. Each stage consists of a TPT Block with a sampling coefficient of n , adjusting the specific time scale through n times sampling modules within the block.

The TPT block first aggregates highly correlated regions through the pre-attention stage, and then extracts features with the refined attention stage at a finer granularity. Specifically, for the TPT block input $X_{in} \in \mathbb{R}^{C \times T \times H/16 \times W/16}$, we first perform n rounds of temporal downsampling, where the temporal information is aggregated at a granularity of 2^n without overlap. The downsampling module consists of a BN layer and a 3D convolution layer with the kernel and stride size of $(2 \times 1 \times 1)$, resulting in an output $X_{sample} \in \mathbb{R}^{C \times T/2^n \times H/16 \times W/16}$.

The temporal difference convolution (TDC) [55] has been proven to effectively capture fine-grained local temporal difference features [53, 56, 57, 60]. We utilize the TDC module for projecting Q and K, while V is projected using linear projection. The projected Q and K are subjected to a 3D average pooling operation to compute attention within a larger spatio-temporal receptive field, which filters out low-correlation key-value pairs. Specifically, for input $Q, K \in \mathbb{R}^{C \times T/2^n \times H/16 \times W/16}$, the pooling convolutional kernel size is $(T' \times H' \times W')$.

$$T' = \lfloor \frac{T}{T_s} \rfloor, H' = \lfloor \frac{H/16}{4} \rfloor, W' = \lfloor \frac{W/16}{4} \rfloor \quad (4)$$

Where $T_s = MAX(2^x, 2^n)$, and x is the partition coefficient. In the experiments, since the frame rate of the dataset is uniformly downsampled to 30, x is set to 2. The number of tokens in the pre-attention is $T_s \times 4 \times 4$. The scores of the pre-attention are computed as follows:

$$Score = Q'(K')^T \quad (5)$$

The pre-attention stage is designed to obtain the indices of top-k positions with high correlation, to filter out low-correlation key-value pairs. The pre-attention captures spatio-temporal correlations within a large receptive field, gathering the regions highly correlated with Q in both K and V. If given a token of the skin area as a query, it corresponds to gathering skin regions with similar temporal phases to the Query. The gathered key and value are expressed as:

$$\begin{aligned} K^g &= gather(K, topkIndex(Score)) \\ V^g &= gather(V, topkIndex(Score)) \end{aligned} \quad (6)$$

The refined attention stage is computed on the top- k (high-correlation) regions identified after the pre-attention gathering. Subsequently, the local positional information is enhanced through a LCE module following self-attention [35, 61]. The i th self-attention head output SA_i is:

$$SA_i = \text{Softmax}(Q(K^g)^T / \sqrt{D}) V^g + \text{LCE}(V) \quad (7)$$

where D represents the dimensionality of single-head attention, and LCE is a 3D convolution with a kernel size of $(3 \times 3 \times 3)$. The output of multi-head self-attention is obtained by concatenating the outputs from all attention heads, followed by a linear projection through the weight matrix $W \in \mathbb{R}^{D \times D}$.

$$MHSA = \text{Concat}(SA_1, SA_2, \dots, SA_h)W \quad (8)$$

Like vanilla transformer [44], residual connection, BN, and feed-forward would be conducted after MHSA. Diverging from that, inspired by [56, 57], an additional hidden layer is incorporated into the feed-forward layer. This hidden layer consists of a three-dimensional convolution, BN, and GELU, intended to refine local inconsistency and reinforce relative position cues. Finally, the Temporal Periodic Transformer will generate output through n temporal up-sampling modules. The dimensionality of the output X_{out} will be restored to match the consistency of the input X_{in} , $X_{out} \in \mathbb{R}^{C \times T \times H/16 \times W/16}$.

3.4. HR Hybrid Loss

Previous loss functions have constrained rPPG signals from both the temporal domain [3, 23, 37, 51] and the frequency domain [32, 39, 53]. Temporal domain constraints primarily operate at the signal-trend level, e.g. the amplitude of the signal. Frequency domain constraints, on the other hand, focus on guiding the learning of periodic features. However, due to the potential mixture of information and noise in the ground truth BVP, there is a gap between the BVP loss and HR metrics during the training process. Therefore, we introduce a loss function that characterizes the HR distance, which is a non-gradient-bearing loss used solely to guide the network in selecting the optimal checkpoint.

Since the collection of ground truth BVP may involve errors, instead of treating HR as a deterministic value, HR is viewed as a probability distribution centered around the HR value. The HR distance is characterized by the distance between the ground truth HR distribution and the predicted HR distribution. Specifically, the HR distribution is expressed by:

$$HR_x = N(\mu, \sigma^2) \quad (9)$$

Where N represents a normal distribution, and x denotes the ground truth or the prediction. And μ denotes the mean of the distribution, where $\mu = \text{maxIdx}(PSD(BVP_x))$.

The maxIdx indicates the index of the maximum value, and PSD indicates the power spectrum. The HR distance is expressed by:

$$\mathcal{L}_{HR} = KL(HR_{gt}, HR_{pred}) \quad (10)$$

The temporal loss \mathcal{L}_{Time} is computed using the negative Pearson correlation coefficient, and the frequency loss is calculated using the cross-entropy between the predicted BVP wave's frequency domain and the heart rate derived from the actual BVP wave. The frequency loss \mathcal{L}_{Freq} is then expressed by:

$$\mathcal{L}_{Freq} = CE(\text{maxIdx}(PSD(BVP_{gt})), PSD(BVP_{pred})) \quad (11)$$

The overall loss is expressed by:

$$\mathcal{L}_{overall} = \alpha * \mathcal{L}_{Time} + \beta * \mathcal{L}_{Freq} + \gamma * \mathcal{L}_{HR} \quad (12)$$

Where $\alpha = 0.2$, $\beta = 1.0$, $\gamma = 1.0$ in our experiment.

4. Experiment

4.1. Dataset and performance metric

Three publicly available datasets were used for evaluation: PURE [40], UBFC-rPPG [2], and MMPD [41]. Specifically, PURE contains 60 1-minute videos comprised of 10 participants engaged in six activities, with a video resolution of 640x480 and a frame rate of 30Hz. UBFC-rPPG contains 42 videos, recording subjects in a stationary state, with a resolution of 640x480 and a frame rate of 30Hz. MMPD comprised 33 participants with Fitzpatrick skin types 3-6. These participants performed four different activities (static, head rotation, speech, and walking) under four lighting conditions (LED-high, LED-low, incandescent, natural). The dataset included 660 1-minute videos with a resolution of 320x240 and a frame rate of 30Hz. Notably, MMPD has two versions: a compressed mini-MMPD and an uncompressed MMPD. In this study, the mini-MMPD was chosen for experimentation. Clearly, among the three datasets, PURE and UBFC are relatively easy, while MMPD stands out with a significantly larger sample size and more complex environment. Five commonly used metrics: Mean Absolute Error (MAE), Root Mean Squared Error (RMSE), Mean Absolute Percentage Error (MAPE), Pearson correlation coefficient (ρ), and Signal-to-Noise Ratio (SNR) were used for evaluation.

4.2. Implementation Details

We leveraged the rPPG toolbox [24], an open-source toolbox based on PyTorch, to implement the proposed method. A comparative analysis was conducted against several state-of-the-art methods, all implemented with the same

Table 1. Intra-dataset results on PURE and UBFC.

Method	PURE			UBFC		
	MAE	RMSE	ρ	MAE	RMSE	ρ
HR-CNN[39]	1.84	2.37	0.98	4.90	5.89	0.64
DeepPhys[3]	0.83	1.54	0.99	6.27	10.82	0.65
SynRhythm[30]	2.71	4.86	0.98	5.59	6.82	0.72
PhysNet[51]	2.10	2.60	0.99	2.95	3.67	0.97
rPPGNet[52]	0.74	1.21	-	0.56	0.73	0.99
Meta-rPPG[17]	2.52	4.63	0.98	5.97	7.42	0.53
TS-CAN[22]	2.48	9.01	0.92	1.70	2.72	0.99
Siamese[42]	0.51	1.56	0.83	0.48	0.97	-
PulseGAN[38]	2.28	4.29	0.99	-	-	-
Dual-GAN[27]	0.82	1.31	0.99	0.44	0.67	0.99
AND-rPPG[26]	-	-	-	2.67	4.07	0.92
TDM[6]	1.83	2.30	0.99	2.32	3.08	0.99
PhysFormer[56]	1.10	1.75	0.99	0.50	0.71	0.99
EfficientPhys[23]	-	-	-	1.14	1.81	0.99
RADIANT[13]	-	-	-	2.91	4.52	-
Li et al.[20]	1.44	2.50	-	0.76	1.62	-
LSTC[18]	-	-	-	0.70	1.00	0.99
zhang et al.[59]	1.53	2.29	0.99	-	-	-
Ours	0.27	0.47	0.99	0.50	0.78	0.99

Table 2. Intra-dataset results on MMPD.

Method	MMPD				
	MAE	RMSE	MAPE	ρ	SNR
DeepPhys[3]	22.27	28.92	23.9	-0.03	-13.44
PhysFormer[56]	11.99	18.41	12.50	0.18	-9.51
EfficientPhys[23]	13.47	21.32	14.19	0.21	-9.25
TS-CAN[22]	9.71	17.22	10.36	0.44	-6.69
PhysNet[51]	4.80	11.80	4.74	0.60	1.77
Ours	3.07	6.81	3.24	0.86	5.46

toolbox. We followed the protocol outlined in [53] by employing random upsampling, downsampling, and horizontal flipping for data augmentation. For each video segment, the facial region was cropped and resized to 128×128 pixels in the first frame, and this region was fixed in the subsequent frames. In post-processing, a second-order Butterworth filter was applied to filter the predicted PPG waveform. The Welch algorithm was then employed to compute the power spectral density for further heart rate estimation. One more thing to note is that due to suboptimal performance on most datasets with PhysFormer’s original configuration, similar to the treatment of PhysNet[51] in the toolbox, we utilized the normalized frame difference as the input for PhysFormer. For a fair comparison, all experiments were conducted under the same experimental setting. Default hyperparameters from the toolbox were employed. The learning rate was set to 9e-3. The batch size was set to 4, and the training process spanned 30 epochs. Network training was conducted on an NVIDIA RTX A6000.

4.3. Intra-dataset evaluation

For the evaluation on the PURE dataset, we adhered to the protocol outlined in [27, 39]. Specifically, the first 60% of the dataset was utilized for training, while the remaining 40% was allocated for testing. Similarly, for the evaluation on the UBFC dataset, we followed the protocol specified in [27, 38], selecting the initial 30 samples for training and the subsequent 12 samples for testing. As illustrated in Table 1, on the PURE dataset, our method outperformed state-of-the-art methods across all metrics. In the case of the UBFC dataset, our method demonstrated comparable performance to state-of-the-art methods.

Since the relative simplicity of PURE and UBFC, the performance of state-of-the-art methods on these two datasets is about to be saturated. We further conducted an evaluation with the challenging MMPD dataset, partitioned into training, validation, and test sets with a ratio of 7:1:2. As depicted in Table 2, we compared our method against existing state-of-the-art approaches. Note that the MMPD dataset is newly published. The performance of existing methods on this dataset is reimplemented by ourselves with the rPPG toolbox. Confronting the more complex environmental conditions of MMPD, our approach achieved the lowest MAE (3.07), RMSE (6.81), and the highest ρ (0.86), surpassing previous approaches by a significant margin. These showcased superior rPPG feature extraction capabilities, demonstrating the enhanced robustness of RhythmFormer.

The observed phenomenon of other Transformer-based methods performing well on PURE and UBFC but showing a large performance margin on MMPD suggests that: in more complex environments, coarse-grained extraction of rPPG features is highly susceptible to noise interference, leading to poor robustness. RhythmFormer leveraging periodic sparse attention for fine-grained extraction of rPPG features, demonstrates its potential for applications in complex real-world environments with outstanding robustness.

4.4. Cross-Dataset Evaluation

In addition, we followed the protocol outlined in [24] for cross-dataset evaluation. The models were trained on PURE and UBFC individually and subsequently tested on PURE, UBFC, and MMPD datasets. The training dataset was split, with the initial 80% used for training and the remaining 20% for validation. Comparative results against state-of-the-art end-to-end methods are presented in Table 3. The results highlight the superior capability of RhythmFormer in modeling domain-invariant rPPG features and its remarkable generalization across diverse datasets.

4.5. Ablation Study

We conducted ablation experiments on the MMPD dataset to assess the impact of different modules.

Table 3. Cross-dataset results.

Method	Train Set	Test Set														
		PURE					UBFC					MMPD				
		MAE	RMSE	MAPE	ρ	SNR	MAE	RMSE	MAPE	ρ	SNR	MAE	RMSE	MAPE	ρ	SNR
GREEN[45]	-	10.09	23.85	10.28	0.34	-2.66	19.73	31.00	18.72	0.37	-11.18	21.68	27.69	24.39	-0.01	-14.34
ICA[34]	-	4.77	16.07	4.47	0.72	5.24	16.00	25.65	15.35	0.44	-9.91	18.60	24.30	20.88	0.01	-13.84
CHROM[9]	-	5.77	14.93	11.52	0.81	4.58	4.06	8.83	3.84	0.89	-2.96	13.66	18.76	16.00	0.08	-11.74
LGI[33]	-	4.61	15.38	4.96	0.77	4.50	15.80	28.55	14.70	0.36	-8.15	17.08	23.32	18.98	0.04	-13.15
PBV[10]	-	3.92	12.99	4.84	0.84	2.30	15.90	26.40	15.17	0.48	-9.16	17.95	23.58	20.18	0.09	-13.88
POS[48]	-	3.67	11.82	7.25	0.88	6.87	4.08	7.72	3.93	0.92	-2.39	12.36	17.71	14.43	0.18	-11.53
DeepPhys[3]	UBFC	5.54	18.51	5.32	0.66	4.40	-	-	-	-	-	17.50	25.00	19.27	0.06	-11.72
	PURE	-	-	-	-	-	1.21	2.90	1.42	0.99	1.74	16.92	24.61	18.54	0.05	-11.53
PhysNet[51]	UBFC	8.06	19.71	13.67	0.61	6.68	-	-	-	-	-	9.47	16.01	11.11	0.31	-8.15
	PURE	-	-	-	-	-	0.98	2.48	1.12	0.99	1.49	13.94	21.61	15.15	0.20	-9.94
TS-CAN[22]	UBFC	3.69	13.80	3.39	0.82	5.26	-	-	-	-	-	14.01	21.04	15.48	0.24	-10.18
	PURE	-	-	-	-	-	1.30	2.87	1.50	0.99	1.49	13.94	21.61	15.15	0.20	-9.94
PhysFormer[56]	UBFC	2.93	10.11	4.80	0.90	9.91	-	-	-	-	-	10.69	17.23	12.48	0.27	-8.84
	PURE	-	-	-	-	-	2.35	6.26	2.32	0.94	2.97	10.49	17.14	11.98	0.32	-8.27
EfficientPhys[23]	UBFC	5.47	17.04	5.40	0.71	4.09	-	-	-	-	-	13.78	22.25	15.15	0.09	-9.13
	PURE	-	-	-	-	-	2.07	6.32	2.10	0.94	-0.12	14.03	21.62	15.32	0.17	-9.95
Ours	UBFC	0.97	3.36	1.60	0.99	12.01	-	-	-	-	-	9.08	15.07	11.17	0.53	-7.73
	PURE	-	-	-	-	-	0.89	1.83	0.97	0.99	6.05	8.98	14.85	11.11	0.51	-8.39

Table 4. Ablation of Fusion Stem.

Input	Stem	MAE	RMSE	MAPE	ρ	SNR
DiffNorm	Vanilla Stem	3.93	8.66	3.98	0.79	3.65
Standard	Vanilla Stem	3.56	7.99	3.71	0.81	3.52
Standard	Fusion Stem	3.07	6.81	3.24	0.86	5.46

Table 5. Effectiveness of Fusion Stem.

Backbone	w/o Fusion Stem			w. Fusion Stem		
	MAE	RMSE	ρ	MAE	RMSE	ρ
DeepPhys[3]	22.27	28.92	-0.03	8.82	16.04	0.39
PhysNet[51]	4.80	11.80	0.60	3.84	9.19	0.74
TS-CAN[22]	9.71	17.22	0.44	6.91	13.71	0.51
PhysFormer[56]	11.99	18.41	0.18	8.72	14.47	0.45
EfficientPhys[23]	13.47	21.32	0.21	6.65	13.20	0.56

Impact of Fusion Stem. As illustrated in Table 4, through the comparison of ablation experiments with different input forms, we validated the effectiveness of the fusion stem. Compared to raw frame input and normalized frame difference input, the fusion stem significantly improves performance. Integrating the difference frame into the raw frame, enables frame-level awareness of BVP wave variations, effectively enhancing rPPG features. This further guides the self-attention mechanism of the transformer to reinforce its focus on rPPG representation.

Furthermore, the fusion stem can be easily applied to other methods. We incorporated the fusion stem into existing methods. As demonstrated in Table 5, the applica-

Table 6. Ablation of Pre-Attention.

Pre-Attention	MAE	RMSE	MAPE	ρ	SNR
w/o	4.43	9.08	4.53	0.76	3.3
w.	3.07	6.81	3.24	0.86	5.46

Table 7. Ablation of Multi-Scale.

Mul-Scale	Strategy	n	MAE	RMSE	MAPE	ρ	SNR
w/o	-	0	4.52	10.24	4.88	0.69	0.89
w/o	-	1	4.90	11.07	4.99	0.65	1.73
w/o	-	2	3.75	8.01	3.86	0.81	2.83
w/o	-	3	4.26	8.85	4.42	0.76	3.57
w.	concat	1,2,3	3.61	7.25	3.83	0.85	0.72
w.	hierar.	3,2,1	5.10	10.73	5.21	0.64	0.96
w.	hierar.	1,2,3	3.07	6.81	3.24	0.86	5.46

tion of the fusion stem to other methods led to significant performance improvements. This strongly attests to the effectiveness of the fusion stem, showcasing its capability to enhance rPPG features and improve signal-to-noise ratio across different methodologies.

Impact of Pre-Attention. The main role of pre-attention is to reduce computational complexity and memory usage. Without pre-attention, a single batch’s memory usage surpasses the 48GB memory of a single RTX A6000, necessitating a reversion to coarse attention. As illustrated in Table 6, the results demonstrate that, with pre-attention, fine-grained rPPG information mining notably enhances modeling capability while mitigating noise interference.

Table 8. Computational Cost.

Method	Param. (M)	MACs (G)
DeepPhys[3]	7.504	120.00
PhysNet[51]	0.70	70.12
TS-CAN[22]	7.504	120.00
PhysFormer[56]	7.381	50.607
EfficientPhys[23]	7.439	60.687
RhythmFormer(ours)	3.251	38.494

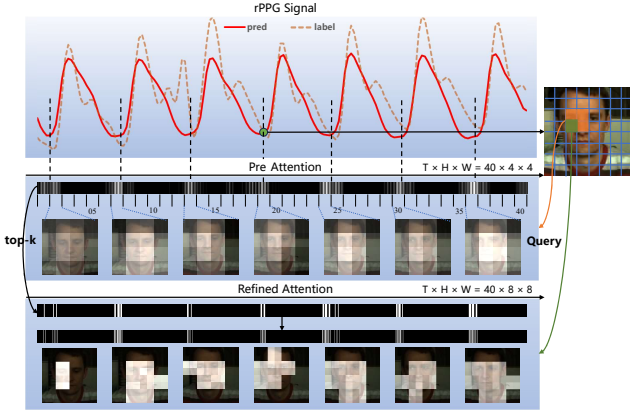


Figure 3. Visualization of attention maps. Given the 294_{th} coarse-grained token in orange as a query for the pre-attention stage, while the 1179_{th} fine-grained token in green as a query for the refined attention stage. The refined attention is calculated in the top-k region obtained from the pre-attention. The figure displays attention score maps and key responses for both two attention stages.

Impact of Multi-Scale. We compared the performance of the model under different fusion strategies and at different temporal scales, as shown in Table 7. The results in the first four rows indicate that, compared to a single scale, multi-scale modeling can more effectively capture the periodic rPPG features. The results in the 5_{th} row suggest that, unlike other periodic tasks (such as action counting [14]), hierarchical feature exploration is more effective than concatenation for extracting rPPG information that is of a single category and exhibits quasi-periodicity. The comparison between the last two rows shows that the multi-scale approach with an increasing temporal granularity is far superior to a decreasing temporal granularity. The findings suggest that reinforcing inter-frame rPPG features at a smaller time scale and then extracting periodic features at a larger time scale can effectively eliminate interference, enhancing the ability of the model to represent rPPG signals.

It is noteworthy that, within a single time scale, the use of a 4-frame granularity is significantly superior to others. Particularly, when the scale is set to 1-frame, i.e., globally attending to the temporal sequence, it incurs substantial memory and computational costs, yet the effect is suboptimal. This suggests that aggregating temporal information effectively enhances rPPG features and prevents noise interference.

4.6. Computational Cost

We also reported the parameters and multiply-accumulates (MACs) for all implemented methods, calculated under a video input size of $160 \times 128 \times 128$ ($T \times H \times W$). The results are presented in Table 8. Our method achieves superior performance with fewer parameters and MACs, showcasing the potential for efficient mobile-level rPPG applications.

4.7. Visualization

As shown in Figure 3, we visualized the periodic sparse attention map. For the pre-attention stage, given a token (the 294_{th}) located at the temporal trough and the spatially left face as a Query. The attention score map and key responses were obtained, where brighter regions indicate stronger attention. It provided the top-k (high-correlation) region for the refined attention stage to delve into rPPG features with finer granularity. For the refined attention stage, a sub-token (the 1179_{th}) of the Query from the pre-attention was used as a Query in the top-k region. The attention score map and key responses were also obtained. As observed in Figure 3, the pre-attention score appropriately concentrates on skin regions with similar temporal phases, accurately expressing the periodic nature of rPPG. However, there are still many non-zero attention scores allocated to irrelevant areas. Refined attention focuses on the top-k regions, aiming to minimize attention on irrelevant areas as much as possible. This concentration of attention enables a more detailed extraction of rPPG features, reducing noise interference, and enhancing the model’s robustness.

5. conclusion

In response to the subtle and periodic nature of rPPG signals, we proposed a method that explicitly leverages periodicity to design the periodic sparse attention mechanism, and combines multi-scale temporal learning to unearth the quasi-periodic patterns in weak signals. This method achieved robust performance in rPPG measurement, surpassing previous state-of-the-art approaches across various datasets, and demonstrated outstanding generalization in cross-dataset evaluation. We envision RhythmFormer to serve as a new baseline in the fully supervised rPPG domain. Moreover, RhythmFormer proves highly effective in heart rate assessment tasks, and future exploration will delve into its feasibility for other tasks involving the extraction of periodic signals.

Acknowledgments This work was supported in part by the National Key Research and Development Program of China (2022ZD0117900), the National Natural Science Foundation of China (62206015, 62227801, U19B2032, U20B2062), the Guangdong Basic and Applied Basic Research Foundation (2021A1515110249), and the Fundamental Research Funds for the Central Universities (FRF-TP-22-043A1).

References

- [1] Anurag Arnab, Mostafa Dehghani, Georg Heigold, Chen Sun, Mario Lučić, and Cordelia Schmid. Vivit: A video vision transformer. In *Proceedings of the IEEE/CVF International Conference on Computer Vision*, pages 6836–6846, 2021. 2
- [2] Serge Bobbia, Richard Macwan, Yannick Benezeth, Alamin Mansouri, and Julien Dubois. Unsupervised skin tissue segmentation for remote photoplethysmography. *Pattern Recognition Letters*, 124:82–90, 2019. 5
- [3] Weixuan Chen and Daniel McDuff. Deepphys: Video-based physiological measurement using convolutional attention networks. In *Proceedings of the European Conference on Computer Vision (ECCV)*, pages 349–365, 2018. 1, 2, 4, 5, 6, 7, 8
- [4] Zhiyang Chen, Yousong Zhu, Chaoyang Zhao, Guosheng Hu, Wei Zeng, Jinqiao Wang, and Ming Tang. Dpt: Deformable patch-based transformer for visual recognition. In *Proceedings of the 29th ACM International Conference on Multimedia*, pages 2899–2907, 2021. 2
- [5] Rewon Child, Scott Gray, Alec Radford, and Ilya Sutskever. Generating long sequences with sparse transformers. *arXiv preprint arXiv:1904.10509*, 2019. 2
- [6] Joaquim Comas, Adria Ruiz, and Federico Sukno. Efficient remote photoplethysmography with temporal derivative modules and time-shift invariant loss. In *Proceedings of the IEEE/CVF Conference on Computer Vision and Pattern Recognition Workshops*, pages 2182–2191, 2022. 2, 6
- [7] Rui Dai, Srijan Das, Kumara Kahatapitiya, Michael S Ryoo, and François Brémond. Ms-tct: multi-scale temporal con- vtrransformer for action detection. In *Proceedings of the IEEE/CVF Conference on Computer Vision and Pattern Recognition*, pages 20041–20051, 2022. 4
- [8] Zihang Dai, Zhilin Yang, Yiming Yang, Jaime G Carbonell, Quoc Le, and Ruslan Salakhutdinov. Transformer-xl: At- tentive language models beyond a fixed-length context. In *Proceedings of the 57th Annual Meeting of the Association for Computational Linguistics*, pages 2978–2988, 2019. 2
- [9] Gerard De Haan and Vincent Jeanne. Robust pulse rate from chrominance-based rppg. *IEEE Transactions on Biomedical Engineering*, 60(10):2878–2886, 2013. 1, 2, 7
- [10] Gerard De Haan and Arno Van Leest. Improved motion ro- bustness of remote-ppg by using the blood volume pulse signature. *Physiological measurement*, 35(9):1913, 2014. 1, 2, 7
- [11] Xiaoyi Dong, Jianmin Bao, Dongdong Chen, Weiming Zhang, Nenghai Yu, Lu Yuan, Dong Chen, and Baining Guo. Cswin transformer: A general vision transformer backbone with cross-shaped windows. In *Proceedings of the IEEE/CVF Conference on Computer Vision and Pattern Recognition*, pages 12124–12134, 2022. 2
- [12] Jingda Du, Si-Qi Liu, Bochao Zhang, and Pong C Yuen. Dual-bridging with adversarial noise generation for domain adaptive rppg estimation. In *Proceedings of the IEEE/CVF Conference on Computer Vision and Pattern Recognition*, pages 10355–10364, 2023. 1, 3
- [13] Anup Kumar Gupta, Rupesh Kumar, Lokendra Birla, and Puneet Gupta. Radiant: Better rppg estimation using sig- nal embeddings and transformer. In *Proceedings of the IEEE/CVF Winter Conference on Applications of Computer Vision*, pages 4976–4986, 2023. 2, 3, 6
- [14] Huazhang Hu, Sixun Dong, Yiqun Zhao, Dongze Lian, Zhengxin Li, and Shenghua Gao. Transrac: Encoding multi- scale temporal correlation with transformers for repetitive action counting. In *Proceedings of the IEEE/CVF Confer- ence on Computer Vision and Pattern Recognition*, pages 19013–19022, 2022. 4, 8
- [15] Jiaqi Kang, Su Yang, and Weishan Zhang. Transppg: Two- stream transformer for remote heart rate estimate. *arXiv preprint arXiv:2201.10873*, 2022. 2
- [16] Jun Kong, Yuhang Bian, and Min Jiang. Mtt: Multi-scale temporal transformer for skeleton-based action recognition. *IEEE Signal Processing Letters*, 29:528–532, 2022. 4
- [17] Eugene Lee, Evan Chen, and Chen-Yi Lee. Meta-rppg: Re- mote heart rate estimation using a transductive meta-learner. In *Computer Vision–ECCV 2020: 16th European Confer- ence, Glasgow, UK, August 23–28, 2020, Proceedings, Part XXVII 16*, pages 392–409. Springer, 2020. 6
- [18] Jun Seong Lee, Gyutae Hwang, Moonwook Ryu, and Sang Jun Lee. Lstc-rppg: Long short-term convolutional net- work for remote photoplethysmography. In *Proceedings of the IEEE/CVF Conference on Computer Vision and Pattern Recognition Workshops*, pages 6014–6022, 2023. 2, 6
- [19] Magdalena Lewandowska, Jacek Rumiński, Tomasz Koce- jko, and Jędrzej Nowak. Measuring pulse rate with a web- cam—a non-contact method for evaluating cardiac activity. In *2011 Federated Conference on Computer Science and In- formation Systems (FedCSIS)*, pages 405–410. IEEE, 2011. 1, 2
- [20] Jianwei Li, Zitong Yu, and Jingang Shi. Learning motion- robust remote photoplethysmography through arbitrary res- olution videos. In *Proceedings of the AAAI Conference on Artificial Intelligence*, pages 1334–1342, 2023. 2, 6
- [21] Xiaobai Li, Jie Chen, Guoying Zhao, and Matti Pietikainen. Remote heart rate measurement from face videos under re- alistic situations. In *Proceedings of the IEEE Conference on Computer Vision and Pattern Recognition*, pages 4264– 4271, 2014. 1, 2
- [22] Xin Liu, Josh Fromm, Shwetak Patel, and Daniel McDuff. Multi-task temporal shift attention networks for on-device contactless vitals measurement. *Advances in Neural Infor- mation Processing Systems*, 33:19400–19411, 2020. 2, 4, 6, 7, 8
- [23] Xin Liu, Brian Hill, Ziheng Jiang, Shwetak Patel, and Daniel McDuff. Efficientphys: Enabling simple, fast and accurate camera-based cardiac measurement. In *Proceedings of the IEEE/CVF Winter Conference on Applications of Computer Vision*, pages 5008–5017, 2023. 2, 5, 6, 7, 8
- [24] Xin Liu, Girish Narayanswamy, Akshay Paruchuri, Xiaoyu Zhang, Jiankai Tang, Yuzhe Zhang, Soumyadip Sengupta, Shwetak Patel, Yuntao Wang, and Daniel McDuff. rPPG- toolbox: Deep remote PPG toolbox. In *Thirty-seventh Con- ference on Neural Information Processing Systems Datasets and Benchmarks Track*, 2023. 5, 6

- [25] Ze Liu, Yutong Lin, Yue Cao, Han Hu, Yixuan Wei, Zheng Zhang, Stephen Lin, and Baining Guo. Swin transformer: Hierarchical vision transformer using shifted windows. In *Proceedings of the IEEE/CVF International Conference on Computer Vision*, pages 10012–10022, 2021. 2, 4
- [26] Birla Lokendra and Gupta Puneet. And-rppg: A novel denoising-rppg network for improving remote heart rate estimation. *Computers in biology and medicine*, 141:105146, 2022. 6
- [27] Hao Lu, Hu Han, and S Kevin Zhou. Dual-gan: Joint bvp and noise modeling for remote physiological measurement. In *Proceedings of the IEEE/CVF Conference on Computer Vision and Pattern Recognition*, pages 12404–12413, 2021. 3, 6
- [28] Hao Lu, Zitong Yu, Xuesong Niu, and Ying-Cong Chen. Neuron structure modeling for generalizable remote physiological measurement. In *Proceedings of the IEEE/CVF Conference on Computer Vision and Pattern Recognition*, pages 18589–18599, 2023. 1
- [29] Daniel McDuff. Camera measurement of physiological vital signs. *ACM Computing Surveys*, 55(9):1–40, 2023. 1
- [30] Xuesong Niu, Hu Han, Shiguang Shan, and Xilin Chen. Synrhythm: Learning a deep heart rate estimator from general to specific. In *2018 24th International Conference on Pattern Recognition (ICPR)*, pages 3580–3585. IEEE, 2018. 2, 6
- [31] Xuesong Niu, Shiguang Shan, Hu Han, and Xilin Chen. Rhythmnet: End-to-end heart rate estimation from face via spatial-temporal representation. *IEEE Transactions on Image Processing*, 29:2409–2423, 2019.
- [32] Xuesong Niu, Zitong Yu, Hu Han, Xiaobai Li, Shiguang Shan, and Guoying Zhao. Video-based remote physiological measurement via cross-verified feature disentangling. In *Computer Vision—ECCV 2020: 16th European Conference, Glasgow, UK, August 23–28, 2020, Proceedings, Part II 16*, pages 295–310. Springer, 2020. 2, 3, 5
- [33] Christian S Pilz, Sebastian Zaunseder, Jarek Krajewski, and Vladimir Blazek. Local group invariance for heart rate estimation from face videos in the wild. In *Proceedings of the IEEE Conference on Computer Vision and Pattern Recognition Workshops*, pages 1254–1262, 2018. 1, 2, 7
- [34] Ming-Zher Poh, Daniel J McDuff, and Rosalind W Picard. Non-contact, automated cardiac pulse measurements using video imaging and blind source separation. *Optics express*, 18(10):10762–10774, 2010. 1, 2, 7
- [35] Sucheng Ren, Daquan Zhou, Shengfeng He, Jiashi Feng, and Xinchao Wang. Shunted self-attention via multi-scale token aggregation. In *Proceedings of the IEEE/CVF Conference on Computer Vision and Pattern Recognition*, pages 10853–10862, 2022. 3, 5
- [36] Ambareesh Revanur, Ananyananda Dasari, Conrad S Tucker, and Laszlo A Jeni. Instantaneous physiological estimation using video transformers. In *Multimodal AI in health-care: A paradigm shift in health intelligence*, pages 307–319. Springer, 2022. 2
- [37] Hang Shao, Lei Luo, Jianjun Qian, Shuo Chen, Chuanfei Hu, and Jian Yang. Tranphys: Spatiotemporal masked transformer steered remote photoplethysmography estimation. *IEEE Transactions on Circuits and Systems for Video Technology*, 2023. 2, 3, 5
- [38] Rencheng Song, Huan Chen, Juan Cheng, Chang Li, Yu Liu, and Xun Chen. PulseGAN: Learning to generate realistic pulse waveforms in remote photoplethysmography. *IEEE Journal of Biomedical and Health Informatics*, 25(5):1373–1384, 2021. 6
- [39] Radim Špetlík, Vojtech Franc, and Jirí Matas. Visual heart rate estimation with convolutional neural network. In *Proceedings of the British Machine Vision Conference, Newcastle, UK*, pages 3–6, 2018. 2, 5, 6
- [40] Ronny Stricker, Steffen Müller, and Horst-Michael Gross. Non-contact video-based pulse rate measurement on a mobile service robot. In *The 23rd IEEE International Symposium on Robot and Human Interactive Communication*, pages 1056–1062. IEEE, 2014. 5
- [41] Jiankai Tang, Kequan Chen, Yuntao Wang, Yuanchun Shi, Shwetak Patel, Daniel McDuff, and Xin Liu. Mmpd: Multi-domain mobile video physiology dataset. In *45th Annual International Conference of the IEEE Engineering in Medicine and Biology Society*, 2023. 5
- [42] Yun-Yun Tsou, Yi-An Lee, Chiou-Ting Hsu, and Shang-Hung Chang. Siamese-rppg network: Remote photoplethysmography signal estimation from face videos. In *Proceedings of the 35th annual ACM symposium on applied computing*, pages 2066–2073, 2020. 2, 6
- [43] Zhengzhong Tu, Hossein Talebi, Han Zhang, Feng Yang, Peyman Milanfar, Alan Bovik, and Yinxiao Li. Maxvit: Multi-axis vision transformer. In *European Conference on Computer Vision*, pages 459–479. Springer, 2022. 2, 4
- [44] Ashish Vaswani, Noam Shazeer, Niki Parmar, Jakob Uszkoreit, Llion Jones, Aidan N Gomez, Łukasz Kaiser, and Illia Polosukhin. Attention is all you need. *Advances in neural information processing systems*, 30, 2017. 2, 5
- [45] Wim Verkrusse, Lars O Svaasand, and J Stuart Nelson. Remote plethysmographic imaging using ambient light. *Optics express*, 16(26):21434–21445, 2008. 1, 2, 7
- [46] Sinong Wang, Belinda Z Li, Madian Khabisa, Han Fang, and Hao Ma. Linformer: Self-attention with linear complexity. *arXiv preprint arXiv:2006.04768*, 2020. 2
- [47] Wenjin Wang, Sander Stuijk, and Gerard De Haan. A novel algorithm for remote photoplethysmography: Spatial sub-space rotation. *IEEE Transactions on Biomedical Engineering*, 63(9):1974–1984, 2015. 1, 2
- [48] Wenjin Wang, Albertus C Den Brinker, Sander Stuijk, and Gerard De Haan. Algorithmic principles of remote ppg. *IEEE Transactions on Biomedical Engineering*, 64(7):1479–1491, 2016. 1, 2, 7
- [49] Wenxiao Wang, Lu Yao, Long Chen, Binbin Lin, Deng Cai, Xiaofei He, and Wei Liu. Crossformer: A versatile vision transformer hinging on cross-scale attention. In *International Conference on Learning Representations, ICLR, 2022*. 2
- [50] Zhuofan Xia, Xuran Pan, Shiji Song, Li Erran Li, and Gao Huang. Vision transformer with deformable attention. In *Proceedings of the IEEE/CVF Conference on Computer Vision and Pattern Recognition*, pages 4794–4803, 2022. 2

- [51] Zitong Yu, Xiaobai Li, and Guoying Zhao. Remote photoplethysmograph signal measurement from facial videos using spatio-temporal networks. In *30th British Machine Vision Conference: BMVC 2019. 9th-12th September 2019, Cardiff, UK*. The British Machine Vision Conference (BMVC), 2019. [2](#), [3](#), [5](#), [6](#), [7](#), [8](#)
- [52] Zitong Yu, Wei Peng, Xiaobai Li, Xiaopeng Hong, and Guoying Zhao. Remote heart rate measurement from highly compressed facial videos: an end-to-end deep learning solution with video enhancement. In *Proceedings of the IEEE/CVF International Conference on Computer Vision*, pages 151–160, 2019. [2](#), [6](#)
- [53] Zitong Yu, Xiaobai Li, Xuesong Niu, Jingang Shi, and Guoying Zhao. Autohr: A strong end-to-end baseline for remote heart rate measurement with neural searching. *IEEE Signal Processing Letters*, 27:1245–1249, 2020. [4](#), [5](#), [6](#)
- [54] Zitong Yu, Xiaobai Li, Pichao Wang, and Guoying Zhao. Transrppg: Remote photoplethysmography transformer for 3d mask face presentation attack detection. *IEEE Signal Processing Letters*, 28:1290–1294, 2021. [2](#)
- [55] Zitong Yu, Benjia Zhou, Jun Wan, Pichao Wang, Haoyu Chen, Xin Liu, Stan Z Li, and Guoying Zhao. Searching multi-rate and multi-modal temporal enhanced networks for gesture recognition. *IEEE Transactions on Image Processing*, 30:5626–5640, 2021. [4](#)
- [56] Zitong Yu, Yuming Shen, Jingang Shi, Hengshuang Zhao, Philip HS Torr, and Guoying Zhao. Physformer: Facial video-based physiological measurement with temporal difference transformer. In *Proceedings of the IEEE/CVF Conference on Computer Vision and Pattern Recognition*, pages 4186–4196, 2022. [2](#), [3](#), [4](#), [5](#), [6](#), [7](#), [8](#)
- [57] Zitong Yu, Yuming Shen, Jingang Shi, Hengshuang Zhao, Yawen Cui, Jiehua Zhang, Philip Torr, and Guoying Zhao. Physformer++: Facial video-based physiological measurement with slowfast temporal difference transformer. *International Journal of Computer Vision*, 131(6):1307–1330, 2023. [2](#), [3](#), [4](#), [5](#)
- [58] Wang Zeng, Sheng Jin, Wentao Liu, Chen Qian, Ping Luo, Wanli Ouyang, and Xiaogang Wang. Not all tokens are equal: Human-centric visual analysis via token clustering transformer. In *Proceedings of the IEEE/CVF Conference on Computer Vision and Pattern Recognition*, pages 11101–11111, 2022. [2](#)
- [59] Xiaobiao Zhang, Zhaoqiang Xia, Lili Liu, and Xiaoyi Feng. Demodulation based transformer for rppg generation and heart rate estimation. *IEEE Signal Processing Letters*, 2023. [2](#), [6](#)
- [60] Yu Zhao, Bochao Zou, Fan Yang, Lin Lu, Abdelkader Nasreddine Belkacem, and Chao Chen. Video-based physiological measurement using 3d central difference convolution attention network. In *2021 IEEE International Joint Conference on Biometrics (IJCB)*, pages 1–6. IEEE, 2021. [2](#), [4](#)
- [61] Lei Zhu, Xinjiang Wang, Zhanghan Ke, Wayne Zhang, and Rynson WH Lau. Biformer: Vision transformer with bi-level routing attention. In *Proceedings of the IEEE/CVF Conference on Computer Vision and Pattern Recognition*, pages 10323–10333, 2023. [2](#), [5](#)

RhythmFormer: Extracting rPPG Signals Based on Hierarchical Temporal Periodic Transformer

Supplementary Material

A. Details of Data Augmentation

As shown in figure a, the heart rate (HR) distribution among the datasets is highly imbalanced, and both the PURE and UBFC datasets have limited amounts of data. Due to this, we employed a random sampling data augmentation strategy during training on PURE and UBFC datasets. For cases where the heart rate, calculated from the ground truth BVP wave, exceeded 90 beats per minute, random downsampling was applied; for rates below 75 beats per minute, random upsampling was performed. Additionally, random horizontal flips were applied to all videos.

B. Ablation study of HR Hybrid Loss

We conducted the ablation study on the MMPD dataset to assess the impact of the HR Hybrid Loss. The incorporation of the proposed HR constraint into the two commonly used losses from previous works. One constrained only in the time domain \mathcal{L}_{MSE} and another employs negative Pearson loss in the time domain and cross-entropy loss in the frequency domain $\mathcal{L}_{Hybrid} = \alpha * \mathcal{L}_{Pearson} + \beta * \mathcal{L}_{CE}$. As shown in Table a, the results demonstrate that the HR Hybrid Loss achieves better performance by mitigating the gap between BVP loss and HR metrics, guiding the network to select a more optimal model.

We also computed the Pearson correlation coefficient between the loss and the metrics on the validation set, resulting in 0.81 for the proposed loss and 0.71 for the baseline. Additionally, as depicted in Figure b, the trend of the proposed loss during the later stages of training notably resembled that of the metrics, both reaching their nadir at the 27th epoch.

C. Visualization of the results

As shown in figure f, we present two examples of HR estimation using the proposed method, comparing the predicted BVP signals and the ground truth BVP signals in both the temporal and frequency domains. The predicted signals exhibit a strong alignment with the ground truth signals in terms of trends, yet they lack detailed high-frequency information.

To further assess the consistency between the predicted HR and the ground truth HR, the Bland-Altman plots for all the face videos across three experiments are respectively depicted in figure c,d,e. From the three figures, it can be observed that the scatter plot aligns overall with the $y = x$ line, the points in the difference plot mostly fall within the confidence interval, but there are still some significant outliers with considerable deviations.

Table a. Ablation of HR Hybrid Loss

loss	UBFC - PURE			MMPD		
	MAE	RMSE	ρ	MAE	RMSE	ρ
\mathcal{L}_{MSE}	2.47	8.80	0.93	3.15	7.10	0.85
$\mathcal{L}_{MSE} + \mathcal{L}_{HR}$	0.99	3.01	0.99	3.15	7.10	0.85
\mathcal{L}_{Hybrid}	1.84	7.82	0.94	3.13	6.98	0.85
$\mathcal{L}_{Hybrid} + \mathcal{L}_{HR}$	0.97	3.36	0.99	3.07	6.81	0.86

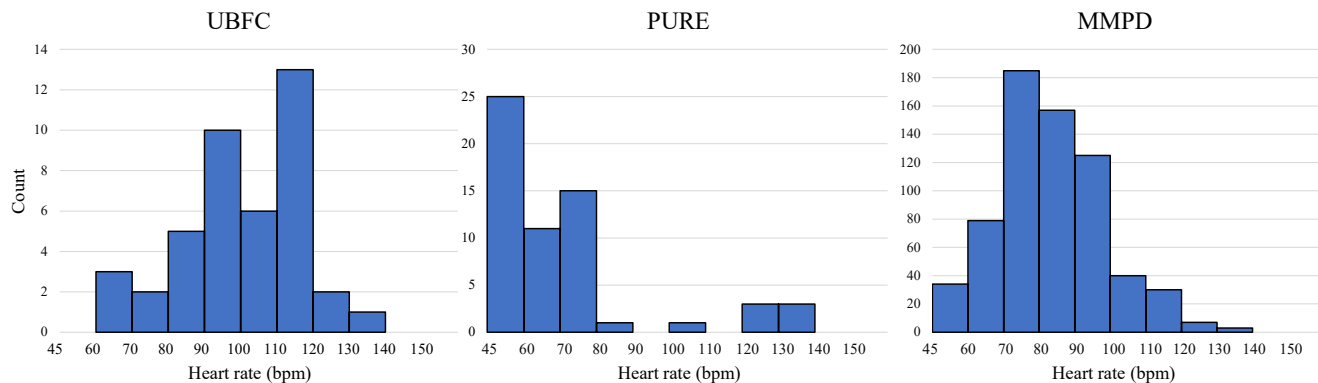


Figure a. Dataset Heart Rate Distribution.

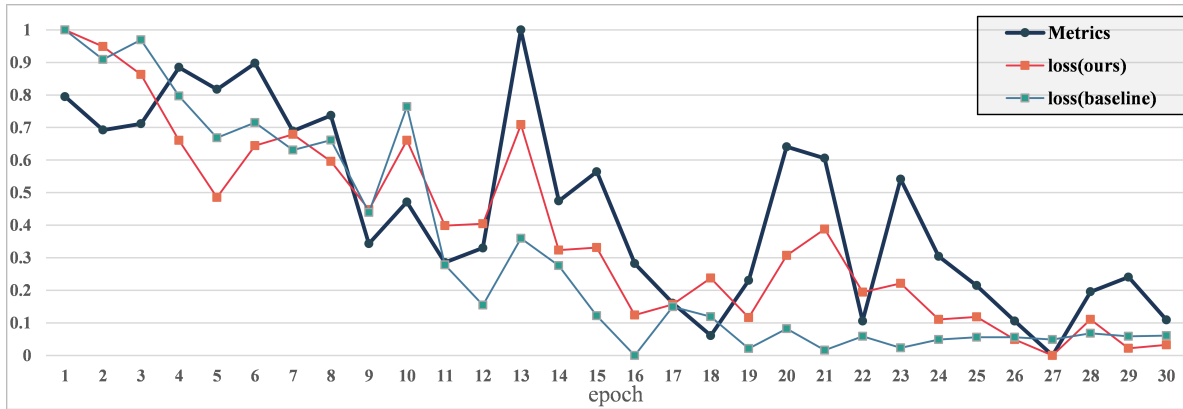


Figure b. Visualization of the training process. The metrics are calculated on the validation set.

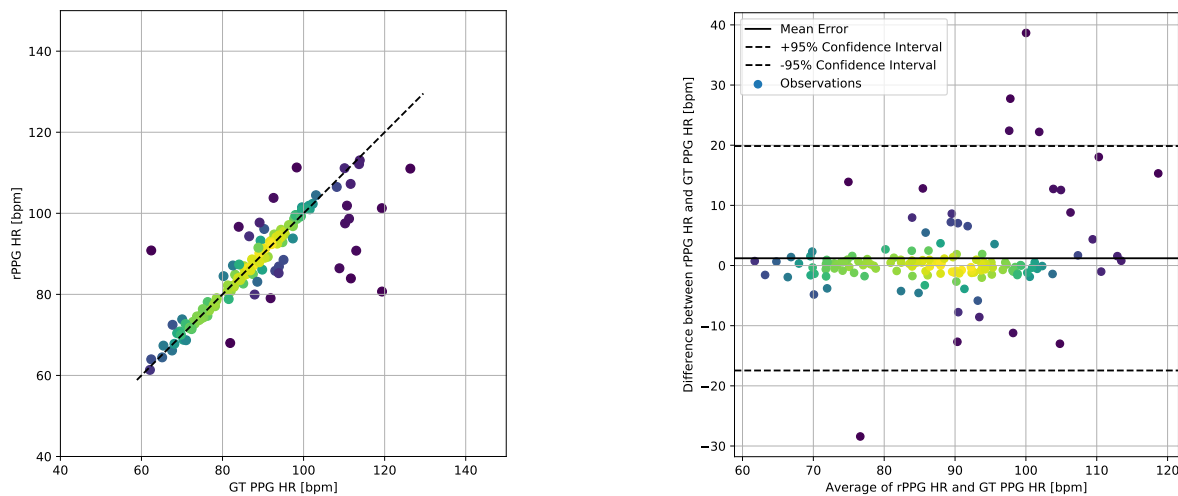


Figure c. The Bland-Altman Plots of Intra-dataset on MMPD.

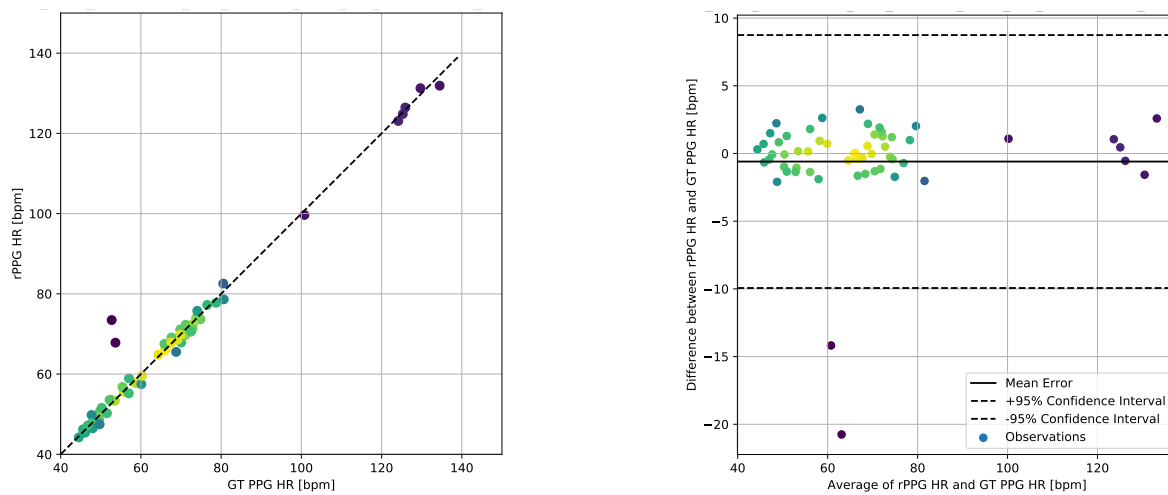


Figure d. The Bland-Altman Plots of training on UBFC and testing on PURE.

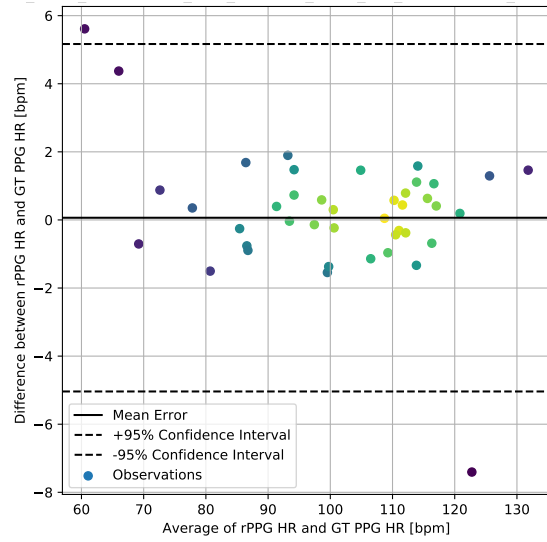
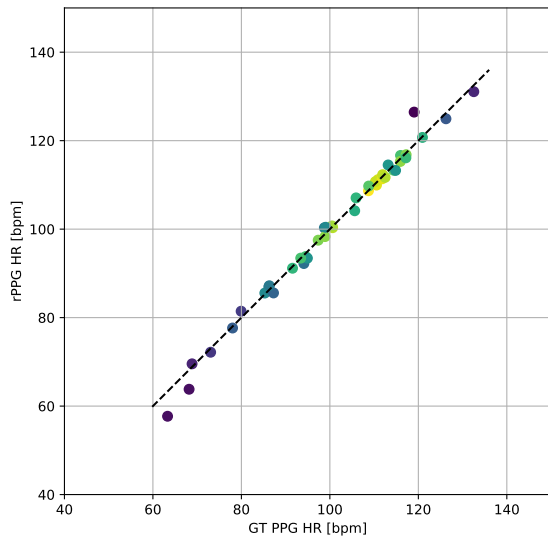
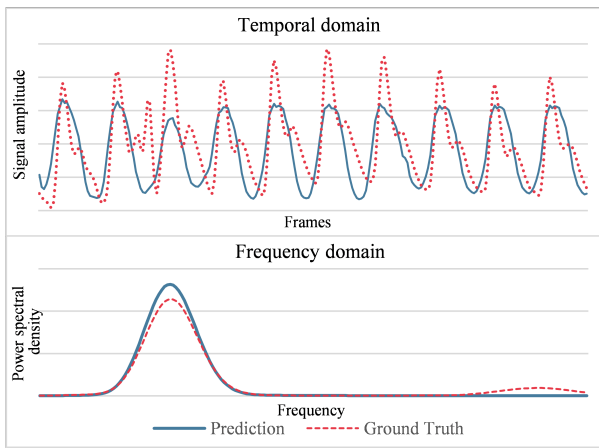
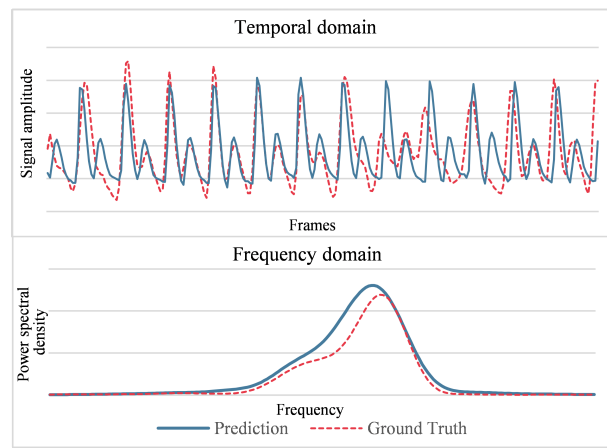


Figure e. The Bland-Altman Plots of training on PURE and testing on UBFC.



(a) A example of Intra-dataset on PURE.



(b) A example of Intra-dataset on MMPD.

Figure f. Two examples of HR estimation using the proposed method. The frequency domain range corresponds to the range of heart rates.